RSC Advances

PAPER

View Article Online
View Journal | View Issue

Cite this: *RSC Adv.*, 2024, **14**, 38806

Study on the discoloration phenomenon caused by iron ion oxidation in Boston ivy pads and its effect on adhesion force†

Rui Zhang,[a] Yida Zhang,[b] Zili Li, *[a] Xiaobin Xu *[a] and Quan Xu *[c]

Boston ivy has received much attention from researchers owing to its exceptional climbing abilities. However, many aspects of their adhesion behavior remain unresolved. Our research has discovered a phenomenon of oxidation and discoloration in Boston ivy pads, which leads to a significant decrease in adhesion force. In this study, we conducted a comprehensive investigation into the oxidation discoloration phenomenon. Through XPS analysis, we confirmed that the transition from Fe^{2+} to Fe^{3+} in the pad is the primary cause of the oxidation discoloration reaction. Furthermore, by conducting *in situ* adhesion testing using AFM, we observed a decrease in adhesion during the oxidation of iron ions. The magnitude of adhesion is closely related to the amount of pyrocatechol. Following the oxidation reaction, iron ions chelate with more pyrocatechol, resulting in a decrease in the available pyrocatechol content for adhesion. To validate this mechanism, we designed and prepared a biomimetic composite adhesion surface of a PDMS hydrogel. This composite surface improved oxidation resistance through the hydrogel, demonstrating improved adhesion performance. These findings offer promising prospects for the application of bionic materials in various fields.

Received 24th June 2024
Accepted 22nd November 2024

DOI: 10.1039/d4ra04605f

rsc.li/rsc-advances

Introduction

There are many organisms with excellent adhesion abilities enabled through physical or chemical mechanisms. Usually, physical adhesion relies on complex hierarchical surfaces and exhibits reversible adhesion properties, such as the feet of geckos.[1–5] Chemical adhesion is often realized by adhesives that are secreted by creatures such as mussels.[6–9] These adhesives offer robust adhesion under damp conditions. In addition to animals, plants also exhibit diverse attachment mechanisms.[10] Unlike animals, plants find it challenging to absorb energy and survive in complex environments. Although pitchers[11,12] and lotus[13,14] have been extensively studied, climbing plants are not fully explored. Research on controllable plant adhesion properties aims to develop complex, adaptable, and energy-efficient biomimetic materials. These materials have potential applications in coatings, building materials, medical facilities,[15] and fiber batteries.[16]

Over the past decades, limited research has been conducted on the adhesion mechanism of Boston ivy (*Parthenocissus tricuspidata*).[17,18] Endress *et al.*[19] found that the surface of immature Boston ivy pads has cuticles, and the adhesive is produced by their epidermal cells, which may be acid polysaccharides. Bowling *et al.*[20] observed that after Boston ivy pads come into contact with an object, their papillary cells could produce an adhesive called rhamnogalacturonan (RG). Steinbrecher *et al.*[21] conducted adhesion force-displacement measurements on various Boston ivy pads to study the optimization of Boston ivy attachment strategies. It was found that the Boston ivy pad structure and adhesive production ability are key to adhesion, but the mechanism needs further validation for more diverse practical applications.

In this study, we investigated the discoloration of Boston ivy pads and its impact on their adhesion mechanism. After the pad is removed, it turns red-brown when exposed to the air, but it does not change color in a nitrogen atmosphere. Combining XPS and AFM characterizations, we found that the discoloration is caused by the oxidation reaction of Fe^{2+} and pyrocatechol, and the adhesion force of the pad decreases as the reaction proceeds. The amount of pyrocatechol that can be used for adhesion is reduced by the chelation of iron ions and oxidation, thus resulting in a decrease in adhesion. We designed a biomimetic adhesive surface based on the morphology and chemical composition of the Boston ivy pad. Inspired by the structure of finger cells on the surface of the Boston ivy pad, a biomimetic surface with a micropillar array was prepared with

[a]*School of Information Science and Technology, Fudan University, Shanghai 200433, China*

[b]*National Synchrotron Radiation Laboratory, University of Science and Technology of China, Hefei, Anhui 230029, China*

[c]*State Key Laboratory of Heavy Oil Processing, China University of Petroleum, Beijing, 102249, China*

† Electronic supplementary information (ESI) available: ESI Fig. S1 to S10. See DOI: https://doi.org/10.1039/d4ra04605f

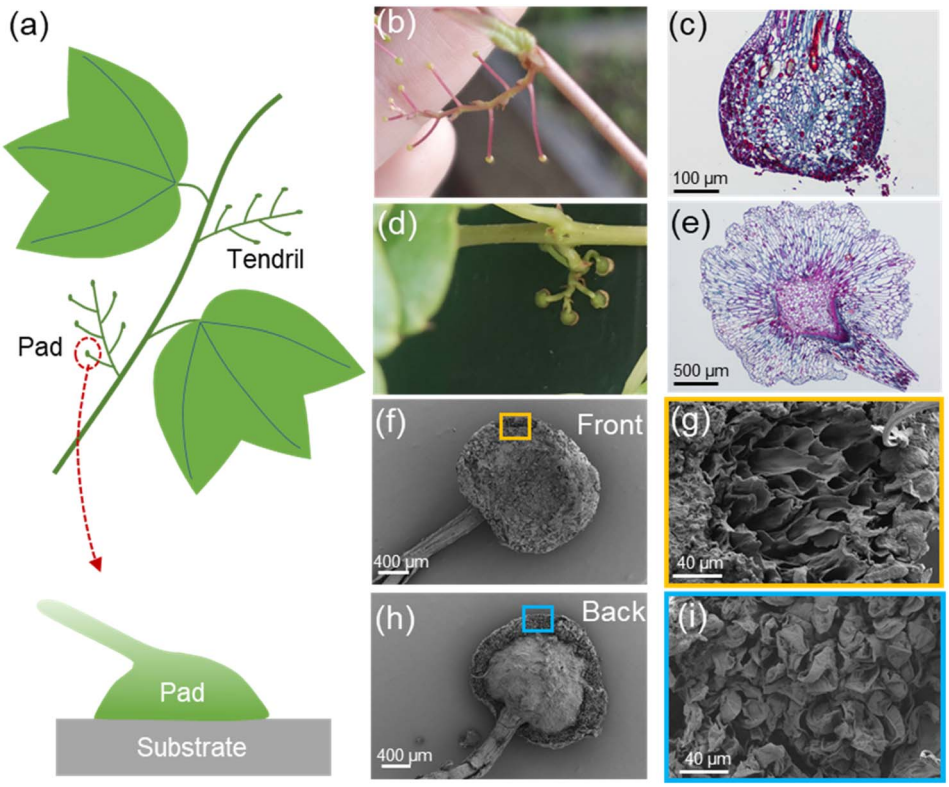

Fig. 1 Structures of the Boston ivy adhesive system: (a) diagram of a part of Boston ivy explaining the relationship of the tendril and adhesive pad (the tip of the tendril). Optical image (b) and micrograph (c) of an immature pad. Image (d) and micrograph (e) of a mature pad. SEM image of the front side of pad (f) and its partially enlarged image of the orange area (g). SEM image of the back side of pad (h) and its partially enlarged image of the blue area (i).

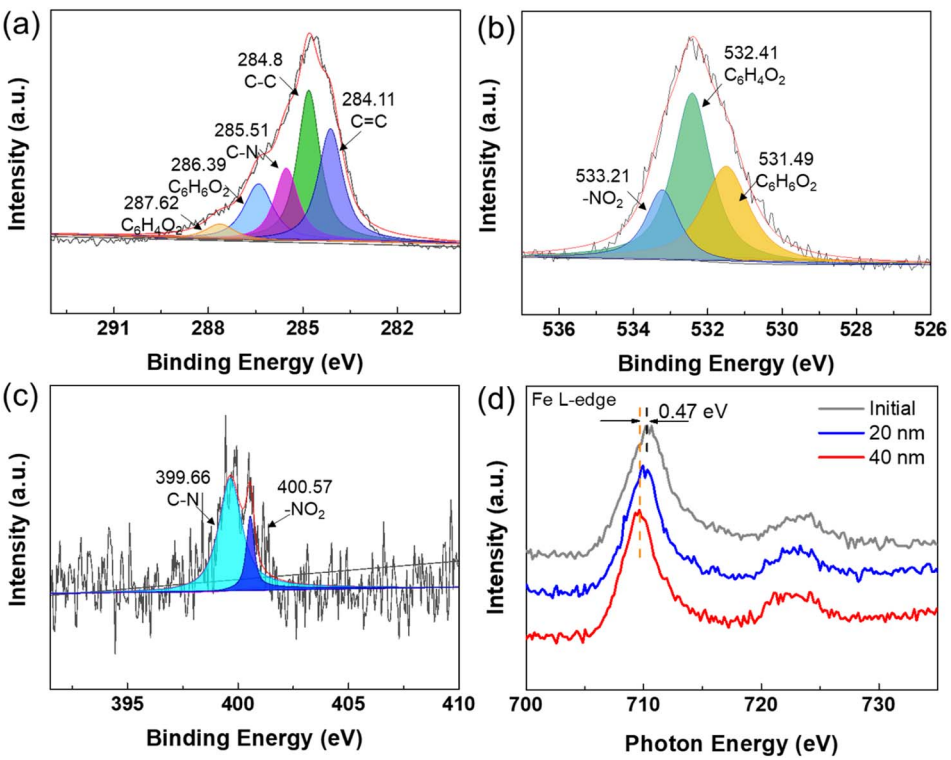

Fig. 2 XANES and XPS analysis of the Boston ivy pad: (a) C 1s, (b) O 1s, and (c) N 1s XPS spectra of the adhesive pad, and (d) XANES spectra mapping of the surface and 20 nm and 40 nm etching on the Boston ivy pad.

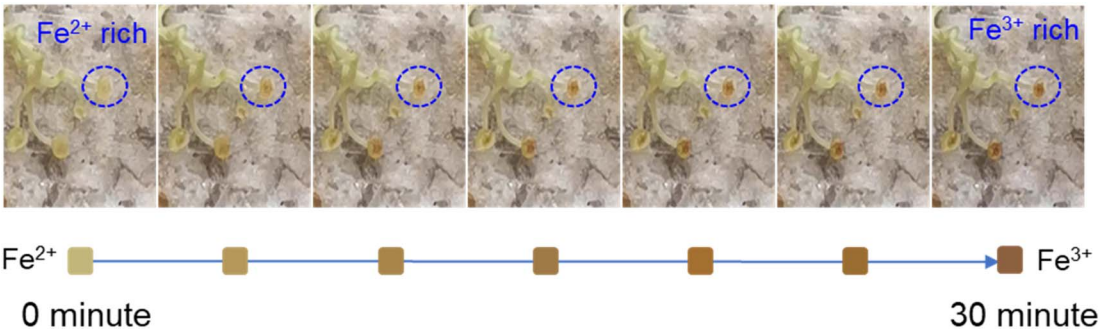

Fig. 3 Optical image of the color change of Boston ivy pads every 5 minutes after removal from the plant. The square shows the color of the pad in the blue circle.

polydimethylsiloxane (PDMS),[22,23] and then, the adhesive on the pad was simulated by a hydrogel,[24–26] forming a composite biomimetic surface.

Results and discussions

Boston ivy plants can climb on almost various types of walls. It sticks to the wall through its tendrils, and the tips of the tendrils transform into attachment pads (Fig. 1a). Each tendril has about 5–8 pads, with a diameter of 1–2 mm. During the growth of Boston ivy plants, the tip of a tendril first swells and has a spherical shape, as shown in Fig. 1b, called immature pads. After contacting the substrate, the pads gradually mature[27] (Fig. 1d), and the tendril stalks contract spirally.[10] Those unattached pads will wither and detach. It is evident from the slice images (Fig. 1c and e) that mature and immature pads exhibit distinct cell shapes. Cells of the immature pad grow rapidly after contacting the substrate, adapting to the shape of the substrate surface and turning into a mature pad. By observing the mature pad under a scanning electron microscope (SEM), it

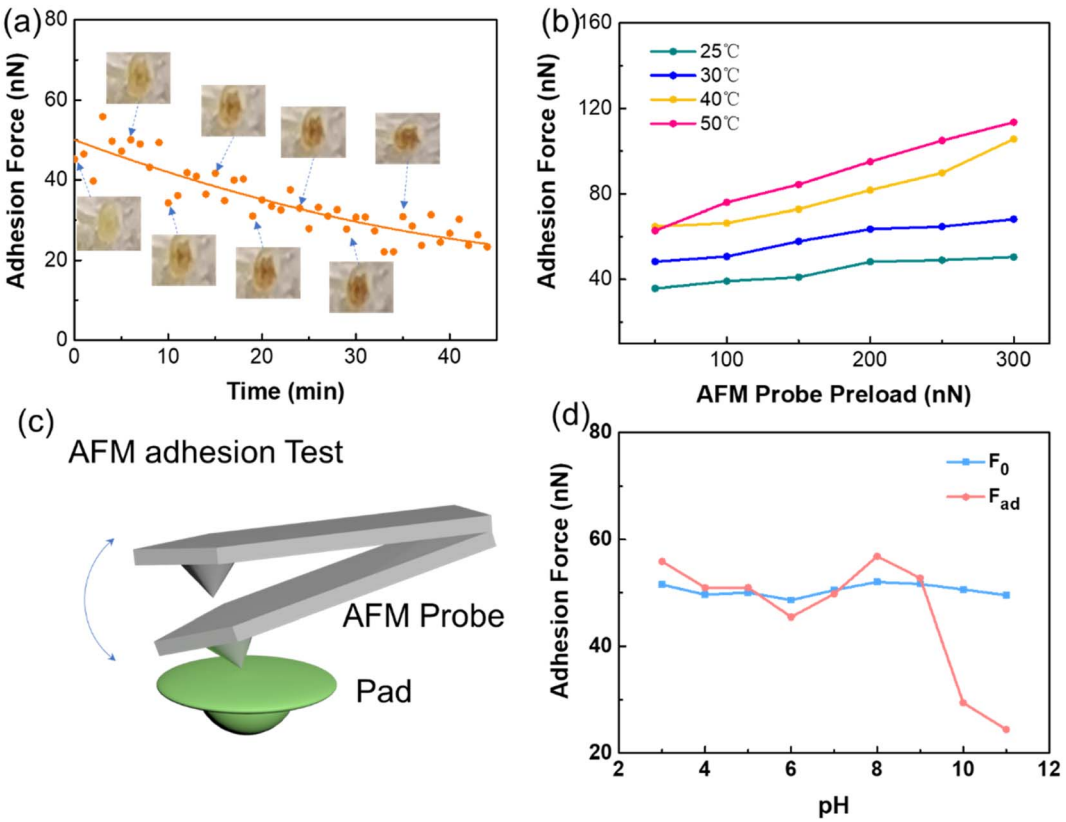

Fig. 4 Adhesion study of Boston ivy pads in different environments: (a) typical adhesion force and color change of a Boston ivy pad with time. (b) Temperature-dependent adhesion force of the Boston ivy pad with different pre-applied compression pressures. (c) Schematic of the typical adhesion force test using an AFM probe. (d) Influence of pH on the adhesion of Boston ivy pad. F_0 and F_{ad} represent the adhesion force of the Boston ivy pad before and after solution treatment with different pH values, respectively.

can be found that there is a layer of tightly arranged cells on the front side (the surface stuck to the substrate) (Fig. 1f), and the interior of the pads is porous after the surface layer is torn (Fig. 1g). The back of the pad is connected to the tendril (Fig. 1h), and has a porous structure (Fig. 1i).

We studied the tensile strength of tendrils, which plays an important role in supporting its weight and resists external influences (such as strong winds). Tensile tests were performed on the Boston ivy's tendrils; the tendrils of mature pads and the tendrils of immature pads are tested separately. The tendrils with mature pads have significantly higher yield stress and strength (Fig. S1†). After the immature pads touch the attachment, the surface cells of the pad will grow and secrete an adhesive to adhere to the substrate.[27] These changes will also affect the tendril and increase its strength.

To understand the chemical mechanism underlying the pad adhesion, we studied the chemical components and molecular structures of Boston ivy pads by X-ray photoelectron spectroscopy (XPS) and X-ray absorption near-edge structure (XANES).

XPS was used to detect the main chemical bonds of the pads. The XPS survey spectrum (Fig. S2†) confirms the presence of C, O, and N elements on the mature pads. From the XPS results (Fig. 2a–c), we can see that C and O are the main elements of the pad, and C–C bonds and C=C bonds account for the highest proportion, which confirm the organic nature of the pads. Most importantly, pyrocatechol and benzoquinone were also detected through XPS. Pyrocatechol is known as an important component in biomimetic adhesive, and it will be partly oxidized to benzoquinone when exposed in air to partially lose adhesion.[28] We believe that pyrocatechol is a key factor to the adhesion mechanism of the pads.

XANES was performed to further study the valence of the Fe ions. Fig. 2d shows the distribution of iron valence on the pad surface and at depths of 20 nm and 40 nm. It can be seen that the peak of 40 nm depth shifts to a low-energy region by 0.4 eV compared with the surface. This indicates that the valence of iron decreases with the increase in etching depth. Fe^{3+} exists more on the surface and Fe^{2+} tends to accumulate in the inside of the Boston ivy pad. This evidence strongly proves that iron ions oxidize less inside the pad the iron oxidation progresses more thoroughly on the surface, and iron ions in the inner part of the pad are exposed to less oxygen and the degree of oxidation is lower.

We found that the Boston ivy pads gradually turned red-brown after leaving the plant. Therefore, we took pictures to record the color change of the pad. As shown in Fig. 3, pictures were taken every five minutes after the tendril was removed from the Boston ivy. In order to see the changes more intuitively, the color of the pad in the blue circle was extracted into the square under every picture. Obviously, the removed pad gradually changed from green to red-brown within 30 minutes. After three hours, the entire tendril will turn red-brown (Fig. S3†), and the tendril will not change color if it is placed in nitrogen (Fig. S4†). It can be seen that air is a necessary factor for color change. Combined with the XPS results, it can be inferred that the color change of the pad is caused by the

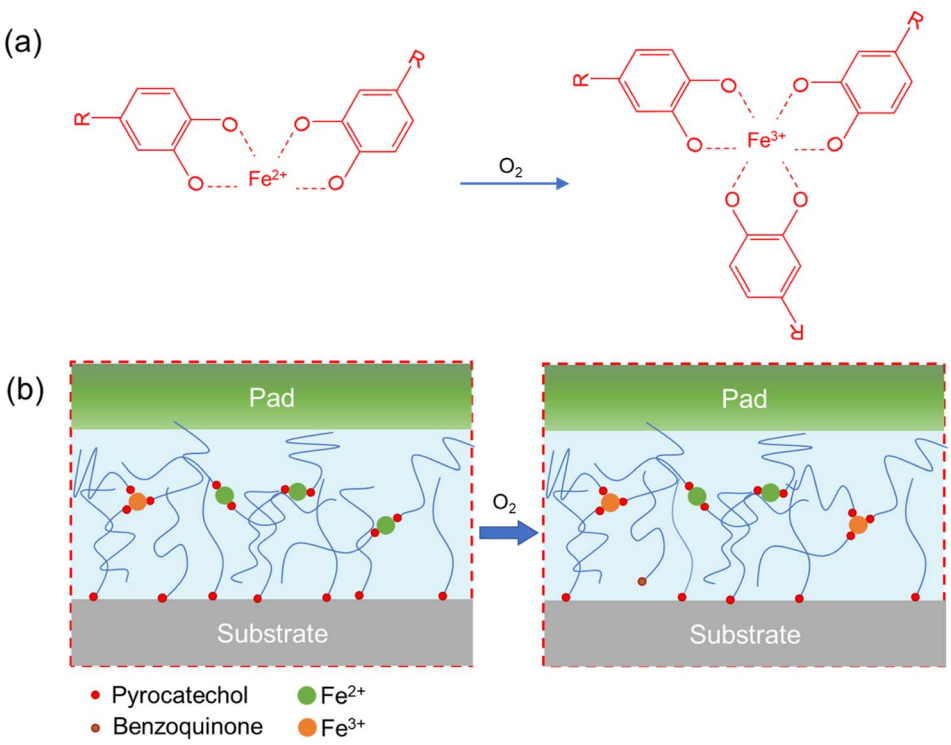

Fig. 5 Molecular reaction mechanisms and their influences on the adhesion behavior of the Boston ivy pads: (a) Fe^{2+} ions were oxidized into Fe^{3+} ions to bond with extra pyrocatechol ligands after the chelate reaction. (b) Schematic showing how the adhesive pyrocatechol ligands detach from their substrate. The oxidation of Fe^{2+} to Fe^{3+} chelates more pyrocatechol, and some pyrocatechol is oxidized to benzoquinone; the content of pyrocatechol on the adhesion surface declines, and the adhesion force decreases.

oxidation of iron ions. The oxygen in the air makes Fe^{2+} react and become Fe^{3+}.

To gain a deeper understanding of the attachment mechanism of Boston ivy plants in different environments, adhesion tests of the surface of a Boston ivy pad were carried out using an atomic force microscope (AFM) (Fig. 4c). As shown in Fig. 4a, we recorded the change in the adhesion force of the pad just after it was removed from the plant, and marked the photo of the pad at different times. It can be seen that the adhesive force of the pad decreases significantly over time, and the downward trend becomes gentle after 30 minutes, which perfectly corresponds to the color change of the pad.

To understand the adhesion mechanism of the pad under different conditions, we tested the adhesion of the pad that has not become red-brown. We recorded the adhesion of the pad at different temperatures. The results are shown in Fig. 4b. As the temperature rises from 25 °C to 50 °C, the adhesion of the Boston ivy pad continues to increase under different preloads. The increasing temperature makes the pad softer and increases the contact area, and hence, the adhesion increases. Therefore, higher temperatures can improve the adhesion effect of pyrocatechol. The adhesion of the pad also increases with the increase in contact time (Fig. S5†). The increase in preload force and contact time both increase the contact area between the AFM tip and pad, resulting in a higher adhesion force.

To study the requirements of the Boston ivy pads for the object, we analyzed the effect of pH on adhesion. The initial adhesion of pads was recorded as F_0, and then the pads were exposed to different pH solutions for 30 minutes respectively. The adhesion force of pads after treatment was recorded as F_{ad}. The test results are shown in Fig. 4d. When the pH is 3–9, the adhesion force does not change significantly. When the pH rises to 10, the adhesion force decreases significantly, which indicates that the alkaline environment will affect the adhesion performance of the pad. This result is consistent with Endress's[19] findings regarding the presence of acidic adhesives in the pad's adhesive.

The oxidation reactions of iron are depicted in Fig. 5a. Fe^{2+} reacts with oxygen to form Fe^{3+} and chelate with three pyrocatechols,[29] thereby consuming a larger portion of pyrocatechol. Moreover, pyrocatechol is oxidized to benzoquinone, which further reduces the available catechol content and, in turn, the adhesion[30] (Fig. 5b). These reactions lead to the pad's color transformation to red-brown and a decrease in the amount of pyrocatechol available for adhesion. Therefore, after the adhesion pad is removed from the plant, the oxidation reactions of Fe^{2+} and pyrocatechol are accelerated, causing the pad change from green to red-brown and resulting in reduced adhesion.

Based on the adhesion mechanism of the Boston ivy pad, we developed biomimetic composite materials (Fig. 6a). The pad's surface cells exhibit a finger-like structure, approximately 10 μm. Polydimethylsiloxane (PDMS) was poured onto a silicon template to make a micropillar array resembling the surface cells (Fig. 6b and e). The space between cells and the interface

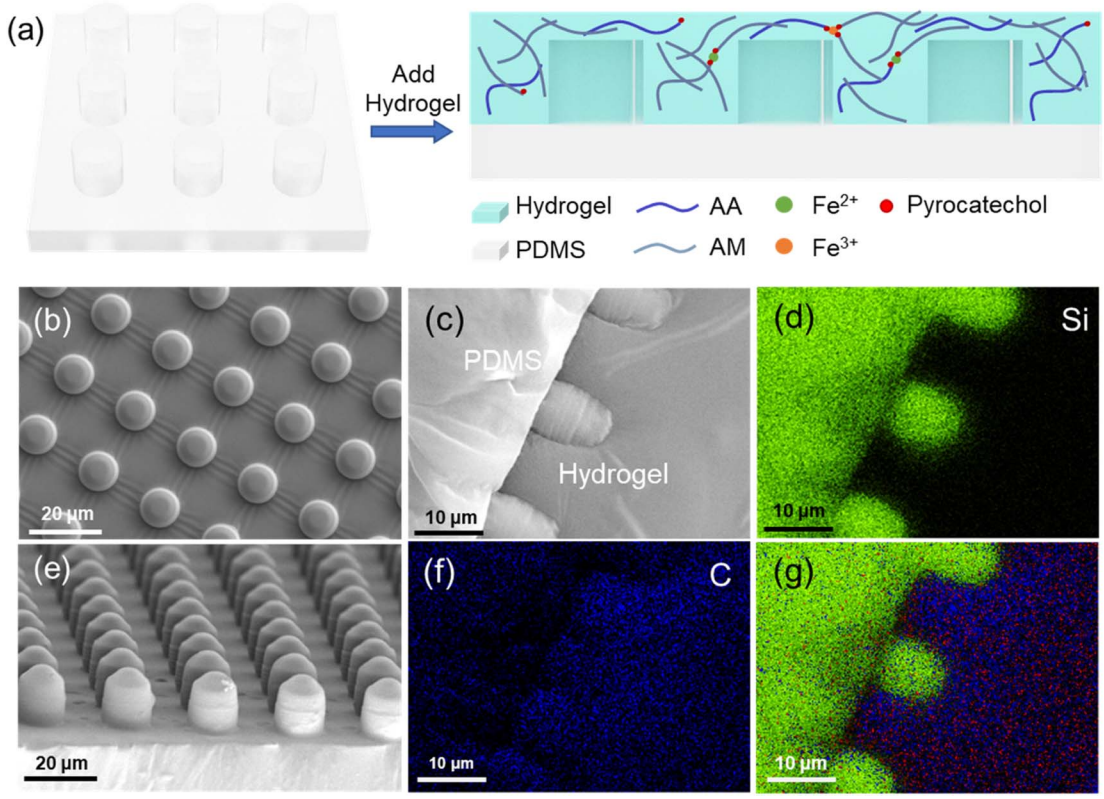

Fig. 6 (a) Fabrication strategy of the biomimetic composite surface: (b) vertical photograph of the biomimetic micropillar array. (c) Cross-sectional image of the composite surface. (d) Distribution of Si element on the composite surface. (e) Cross-sectional photograph of the biomimetic micropillar array. (f) Distribution of C element on the composite surface. (g) Elemental mapping images of the composite surface.

between the pad surface and the substrate is filled with the adhesive,[31] and the hydrogel was used to simulate the adhesive produced by the pad. PDMS is a hydrophobic surface, so it needs to be modified by doping with polyethylene glycol octylphenyl ether (Triton TX-100) during PDMS solidification. The contact angle of PDMS is 107.3°, while that of PDMS doped with TX-100 is 73.95° (Fig. S6†). After ten minutes, the contact angle of PDMS doped with TX-100 will decrease to less than 30°.[32] To facilitate the analysis of the composite surface's integration, it was dried and sectioned, as shown in Fig. 6c. Fig. 6g shows the EDS image of PDMS-hydrogel composite surface, green, blue, and red representing Si, C, and Fe elements respectively. Si is the unique element of PDMS, Fe is the unique element of hydrogel, and C is more distributed in the hydrogel. The content of Fe element in the hydrogel is small and difficult to observe. The element distribution of Si and C elements (Fig. 6d and f) indicates a well-combined interface between PDMS and the hydrogel.

We fabricated four types of hydrogels with different compositions (Fig. S7†) to make biomimetic composite surfaces. The pre-polymerization solution also changed color in air, and the Fe^{3+} pre-polymerization solution shows little color change in half an hour in air, far less than the $Fe^{2+}Fe^{3+}$ pre-polymerization solution (Fig. S8†). The PDMS micropillar array exhibits an adhesion force of approximately 416 nN, while the average adhesion force of PDMS-TX100 is 480 nN (Fig. 7a). The adhesion of hydrogels with different compositions was tested after they were combined with the surface of PDMS-TX100, as shown in Fig. 7b. The adhesion force of tannic acid hydrogel composite surface is slightly higher than that of the dopamine hydrogel, with an average adhesion increase of 20%. The adhesion force of the composite surface doped with Fe^{2+} has been significantly improved, from 947 nN to 1539 nN, with an increase of 60%. This improvement is attributed to the increased hydrogen bonding between pyrocatechol in the hydrogel, enhancing adhesion. Therefore, the composite surface of the TA-$Fe^{3+}Fe^{2+}$-PAAAM hydrogel combined with PDMS has the highest adhesion force, which is consistent with the adhesion mechanism of the Boston ivy pad. Although the TA-$Fe^{3+}Fe^{2+}$-PAAAM hydrogel has a lower tensile strength (Fig. S9†), the strength of composite surface will not be affected due to the PDMS micropillar.

Further investigations were conducted to assess the impact of environmental factors on the composite biomimetic surface. As shown in Fig. 7c, when the temperature rises from 20 °C to 30 °C, the adhesion force increases from 1300 nN to 1450 nN, with a growth rate of about 11%. When the temperature range is between 35 °C and 50 °C, the effect on adhesion force is less pronounced, which is different from the trend tested on Boston ivy pads. It is speculated that the hydrogel is easy to lose water at a higher temperature, thereby reducing the adhesion.

Then the changes in the adhesion force of biomimetic composite surfaces exposed to air were studied. After the preparation of the biomimetic surface is completed, it is

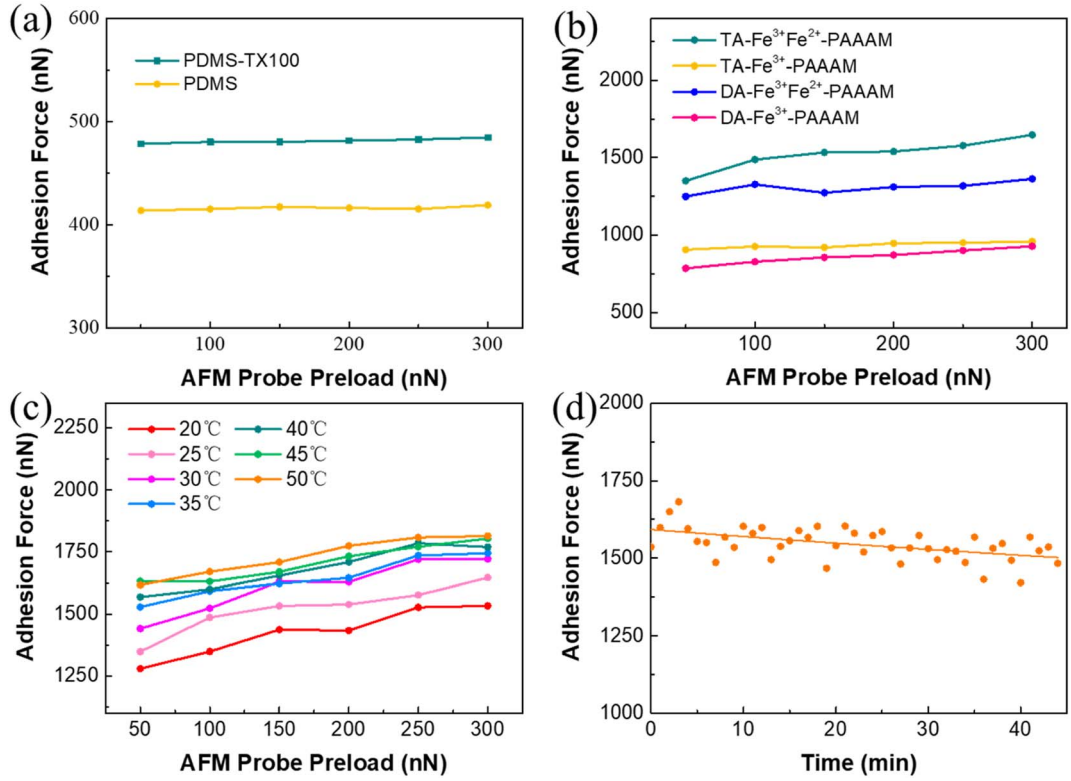

Fig. 7 (a) Adhesion of PDMS under different preloads. (b) Adhesion of different components of the hydrogel composite surface under different preload pressures. (c) Adhesion of the composite surface under different preload pressures and different temperatures. (d) Relationship between the adhesion of the biomimetic surface and the time of exposure to the air.

immediately placed under an AFM to measure the change in the adhesion force on the surface every minute after it is exposed to the air. As shown in Fig. 7d, the adhesion force of the biomimetic composite surface remains relatively stable over time, only decreases by 6% after 45 minutes. This gradual decline of adhesion is related to the water loss of the hydrogel and the oxidation of Fe^{2+}. The composite surface with only Fe^{3+} has a much smaller decrease in adhesion force (Fig. S10†) because there is no oxidation of iron ions, proving that the oxidation of Fe^{2+} is the main reason for the decrease in adhesion. Compared with natural pads, the hydrogel can prevent the penetration of oxygen from air, and hence, the adhesion is less likely to decline. It demonstrates that the composite surface has better stability, and exposure to air does not lead to a significant decrease in adhesion due to rapid oxidation.

Conclusion

In this study, we observed the color transformation of the adhesive pad and identified the presence of pyrocatechol within the pad, along with a gradient distribution of Fe^{3+} and Fe^{2+} across the thickness of the pad. We examined the adhesive properties of the pad and observed a decline in adhesion force as the oxidation reaction progressed. Higher temperatures were found to enhance the pad's adhesion, whereas a highly alkaline environment was detrimental to its adhesive properties. Our findings indicate that Fe^{2+} and pyrocatechol would oxidize with air after the pad is removed, primarily accounting for the pad's color change and the reduction in adhesion force. We employed PDMS-TX100 to mimetic the 'finger cell' structure of the pad, and a hydrogel incorporating iron ions and pyrocatechol was utilized to simulate the adhesive layer on the pad. The test showed that the adhesion of the TA-$Fe^{3+}Fe^{2+}$-PAAAM hydrogel with PDMS-TX100 exhibits the highest adhesion, representing a threefold increase compared to the PDMS surface alone. The biomimetic surface not only exhibits excellent adhesive properties but also demonstrates superior resistance to oxidation over the natural Boston ivy pads. The adhesion of the composite biomimetic surface remains largely unaffected by exposure to air, exhibiting a minimal decline. These insights significantly contribute to the understanding of the Boston ivy's adhesion mechanism and hold promise for inspiring the design and fabrication of bio-inspired adhesive materials.

Experimental details

Materials

Acrylamide (AM), dopamine hydrochloride (DA), tannic acid (TA), acrylic acid (AA), Triton TX-100, trimethylchlorosilane, and *N*,*N*-methylene bisacrylamide (BIS) were purchased from Aladdin. PDMS was purchased from Dow Corning. Ammonium persulfate (APS) was purchased from Beijing Chemical Industry.

Preparation of Boston ivy tendrils

The Boston ivy tendril used in the experiment was obtained from the Boston ivy grown in Beijing, China. The tendrils were cut directly from the plants so that they do not get lignified during the experiment. All the tendrils were preserved in a nitrogen atmosphere. Before the experiment, the sample was ultrasonically cleaned with deionized water to remove impurities.

Preparation of the biomimetic composite surface

The silicon template was cleaned with acetone and isopropanol separately by ultrasonic cleaning for 5 minutes and then dried with nitrogen gas. The silicon template was put into a closed container and 1 mL of trimethylchlorosilane was added. It was heated in an oven at 60 °C for 30 minutes to evenly coat the surface of the silicon template, facilitating subsequent demolding. Then 3% Triton TX-100 was added to PDMS, stirred with a magnetic stirrer at 500 rpm for five minutes, and then mixed with PDMS and a curing agent in a mass ratio of 10/1. The prepared PDMS was poured onto a silicon template, kept under vacuum for thirty minutes in a vacuum tank to ensure the removal of any bubbles inside the PDMS, and then cured at 70 °C for six hours. After PDMS curing is over, it was peeled off from the silicon template to form a biomimetic surface micropillar array. Then 25 mL deionized water was poured into a beaker, different proportions of ferric chloride powder and ferrous chloride powder were added, and then 0.012 g dopamine hydrochloride or 0.008 g tannic acid was weighed and added under stirring using a magnetic stirrer at 500 rpm for five minutes to form a pre-polymerization solution. Then 5.4 g acrylamide (AM), 5.4 mL acrylic acid (AA), and 0.05 g *N*,*N*-methylene bisacrylamide (BIS) were added and stirred using a magnetic stirrer at 500 rpm for 10 minutes to fully dissolve them to form a hydrogel solution. The hydrogel solution was poured onto the surface of the PDMS micropillar array and kept under vacuum in a vacuum tank for 30 minutes to ensure that the bubbles inside the hydrogel solution were removed. Then 0.08 g ammonium persulfate (APS) and 1 mL deionized water were added into the hydrogel solution and fully mixed to obtain the hydrogel. The hydrogel was washed three times with deionized water to remove the remaining ions on its surface.

Preparation of pad for light microscopy

A microtome (RM2016, Leica, Shanghai) was used to slice the pad on the tendril. After that, the sections were infiltrated with xylene for 20 min and ethanol for 10 min, and then they were dehydrated in 95%, 90%, 80%, and 70% alcohol for 5 minutes after dehydrating for 10 minutes in absolute ethanol. They were dyed with 1% saffron dye for one hour and excess dye was washed off with deionized water. After that, they were decolorized with 50%, 70%, and 80% alcohol for 1 min each. Then they were dyed in 0.5% fast green dye solution for 40 seconds and decolorized in ethanol for 1 minute. After the transparency of dimethylbenzene for 5 minutes, the slice was sealed by neutral gum. Photographs were acquired using an optical microscope (NIKON ECLIPSE CI, Japan).

Preparation of the pad for scanning electron microscopy

The pad was fixed in 2.5% glutaraldehyde for four hours, washed four times with a phosphate buffer solution (0.1 M, pH

7.2–7.4), fixed with 1% osmic acid, and then washed four times with a phosphate buffer solution. Then the pad was dehydrated and soaked in 30, 50, 70, 90, 95, and 100% ethanol, ethanol : acetone = 1 : 1, and 100% acetone for 20 minutes. The pad was immersed in 100% acetone : Epon 812 = 2 : 1 for 4 hours and 100% acetone : Epon 812 = 1 : 2 for 4 hours. The sample was observed using a scanning electron microscope (SEM, SU8010).

XPS and XANES analysis

XANES and XPS spectra experiments were conducted at the photoemission end-station at beamline BL10B in the National Synchrotron Radiation Laboratory (NSRL) in Hefei, China. The high-pressure reactor performs *in situ* high-pressure experiments under different atmospheric conditions, which have a maximum range of 2 MPa and a highest temperature of 650 °C. The Fe XANES spectra of different depths in the pad used nitrogen etching to make 20 nm and 30 nm holes and tested the spectra of Fe.

Adhesion test of sample

An Atomic Force Microscope (Dimension Icon AFM, Bruker) was used to test the micro adhesion of the sample under different conditions. The spring constant of the probe used is 3.8 N m^{-1} (MESP-HM, Bruker). The adhesion test of the sample was conducted on different positions of the surface every minute. For the pH influence test, different tendrils were put in different pH solutions for half an hour and then washed with deionized water. Unless otherwise noted, all adhesion tests were conducted under nitrogen to isolate the interference of air.

Data availability

The data supporting this article have been included as part of the ESI.†

Conflicts of interest

The authors declare no competing financial interest.

Acknowledgements

The authors would like to acknowledge the support from the National Natural Science Foundation of China (No. U20A20227).

References

1 K. Autumn, Y. A. Liang, S. T. Hsieh, W. Zesch, W. P. Chan, T. W. Kenny, R. Fearing and R. J. Full, *Nature*, 2000, **405**, 681–685.
2 Y. Tian, N. Pesika, H. Zeng, K. Rosenberg, B. Zhao, P. Mcguiggan, K. Autumn and J. Israelachvili, *Proc. Natl. Acad. Sci. U. S. A.*, 2006, **103**, 19320–19325.
3 H. Peisker, J. Michels and S. N. Gorb, *Nat. Commun.*, 2013, **4**, 1661.
4 L. Qu, L. Dai, M. Stone, Z. Xia and Z. L. Wang, *Science*, 2008, **322**, 238–242.
5 Q. Xu, Y. Wan, T. S. Hu, T. X. Liu, D. Tao, P. H. Niewiarowski, Y. Tian, Y. Liu, L. Dai, Y. Yang and Z. Xia, *Nat. Commun.*, 2015, **6**, 8949.
6 M. J. Harrington, A. Masic, N. Holten-Andersen, J. H. Waite and P. Fratzl, *Science*, 2010, **328**, 216–220.
7 T. Priemel, E. Degtyar, M. N. Dean and M. J. Harrington, *Nat. Commun.*, 2017, **8**, 14539.
8 J. Li, A. D. Celiz, J. Yang, Q. Yang, I. Wamala, W. Whyte, B. R. Seo, N. V. Vasilyev, J. J. Vlassak, Z. Suo and D. J. Mooney, *Science*, 2017, **357**, 378–381.
9 D. E. Fullenkamp, D. G. Barrett, D. R. Miller, J. W. Kurutz and P. B. Messersmith, *RSC Adv.*, 2014, **4**, 25127–25134.
10 S. Junker, *New Phytol.*, 1976, **77**, 741–746.
11 H. Chen, P. Zhang, L. Zhang, H. Liu, Y. Jiang, D. Zhang, Z. Han and L. Jiang, *Nature*, 2016, **532**, 85–89.
12 T.-S. Wong, S. H. Kang, S. K. Y. Tang, E. J. Smythe, B. D. Hatton, A. Grinthal and J. Aizenberg, *Nature*, 2011, **477**, 443–447.
13 Z. Huang, Z. Zhao, S. Zhao, X. Cai, Y. Zhang, Z. Cai, H. Li, Z. Li, M. Su, C. Zhang, Y. Pan, Y. Song and J. Yang, *ACS Appl. Mater. Interfaces*, 2021, **13**, 53242–53251.
14 F. Zhu, *Food Hydrocolloids*, 2017, **63**, 332–348.
15 A. W. Zia, R. Liu and X. Wu, *Bio-Des. Manuf.*, 2022, **5**, 757–785.
16 C. Lu, H. Jiang, X. Cheng, J. He, Y. Long, Y. Chang, X. Gong, K. Zhang, J. Li, Z. Zhu, J. Wu, J. Wang, Y. Zheng, X. Shi, L. Ye, M. Liao, X. Sun, B. Wang, P. Chen, Y. Wang and H. Peng, *Nature*, 2024, **629**, 86–91.
17 C. Darwin, *On the Movements and Habits of Climbing Plants*, 1865.
18 A. G. Endress and W. W. Thomson, *Protoplasma*, 1976, **88**, 315–331.
19 A. G. Endress and W. W. Thomson, *Can. J. Bot.*, 1977, **55**, 918–924.
20 A. J. Bowling and K. C. Vaughn, *Am. J. Bot.*, 2009, **96**, 719–727.
21 T. Steinbrecher, E. Danninger, D. Harder, T. Speck, O. Kraft and R. Schwaiger, *Acta Biomater.*, 2010, **6**, 1497–1504.
22 Y. Zhou, F. Fan, Y. Liu, S. Zhao, Q. Xu, S. Wang, D. Luo and Y. Long, *Nano Energy*, 2021, **90**, 106613.
23 X. Shi, L. Yang, S. Li, Y. Guo and Z. Zhao, *Nano Res.*, 2023, **16**, 6840–6848.
24 Z. Chen, J. Shen, M. Wei, W. Yan, Q. Yan, Z. Li, Y. Chen, F. Zhang, L. Du, B. Yuan and Y. Jin, *Bio-Des. Manuf.*, 2023, **6**, 439–450.
25 F. Rahimi, N. Ahmadkhani, A. Goodarzi, F. Noori, S. Hassanzadeh, S. Saghati, M. Khanmohammadi and A. Goodarzi, *Bio-Des. Manuf.*, 2023, **6**, 284–297.
26 Y. Hong, Z. Lin, Z. Luo, T. Jiang, J. Shang and Y. Yang, *Bio-Des. Manuf.*, 2022, **5**, 729–756.
27 T. Steinbrecher, G. Beuchle, B. Melzer, T. Speck, O. Kraft and R. Schwaiger, *Int. J. Plant Sci.*, 2011, **172**, 1120–1129.

28 B. P. Lee, P. B. Messersmith, J. N. Israelachvili and J. H. Waite, *Annu. Rev. Mater. Res.*, 2011, **41**, 99–132.
29 W. Li, W. Bing, S. Huang, J. Ren and X. Qu, *Adv. Funct. Mater.*, 2015, **25**, 3775–3784.
30 B. K. Ahn, D. W. Lee, J. N. Israelachvili and J. H. Waite, *Nat. Mater.*, 2014, **13**, 867–872.
31 A. J. Bowling and K. C. Vaughn, *Protoplasma*, 2008, **232**, 153–163.
32 J. Seo and L. P. Lee, *Sens. Actuators, B*, 2006, **119**, 192–198.